Vortex force map for multi-body flows with application to wing-flap configurations

Yinan Wang[2], Xiaowei Zhao[3], Michael Graham[4] and Juan Li[1]†,

[1]Department of Engineering, King's College London, London WC2R 2LS, UK
[2]School of Engineering, University of Liverpool, Liverpool L69 3BX, UK
[3]School of Engineering, The University of Warwick, Coventry CV4 7AL, UK
[4]Department of Aeronautics, Imperial College, London SW7 2BY, UK

(Received xx; revised xx; accepted xx)

The vortex force map method for multi-body viscous flows is derived in this work. Extended from and similar to the vortex force map method for a single body in previous work, this approach considers all three force components: the vortex-pressure force, the viscous-pressure force, and the skin friction force. Vortex pressure force maps for each body are designed to identify the force contribution of a given vortex in the flow field and define the positive and negative force-generating critical regions or directions. This multi-body vortex force decomposition method is applied to a wing-flap starting flow problem and validated against computational fluid dynamics. It is found that the dominant force is the vortex-pressure force. And for both the main airfoil and the flap, the force variation against time is closely related to the evolution of the vortex structure near the wing-flap configuration.

Key words: Vortex force map, unsteady flow, viscous flow, force decomposition

1. Introduction

The relationship between the flow structure (such as the velocity and vorticity field) and forces acting on the body has attracted interest for a long time (Polhamus 1966; WANG 2005; Li *et al.* 2018). Unsteady force approaches explaining this relationship are useful in understanding the physical mechanisms in natural flows, especially where vortical flow dominates, such as fish locomotion (Wu 2011), flying seeds (Cummins *et al.* 2018), insects' and birds' wings (Bomphrey *et al.* 2017; Usherwood *et al.* 2020), as well as in engineering problems such as dynamic stall (Li & Feng 2022), design and optimization of air vehicles (Alejandro *et al.* 2018), cars (Liu *et al.* 2021), wind turbines (Dong *et al.* 2022) and so forth. Aside from being a theoretical point of interest, exploring the numerical connection between flow field and fluid forces has practical applications in experimental techniques such as particle image velocimetry (PIV) (Bird *et al.* 2022). Here it may be difficult to obtain accurate flow information near solid surfaces compared to those in numerical simulations, limiting the use of pressure-based fluid force computations and hence necessitating the development of unsteady force methods.

A number of such approaches exist to extract aerodynamic and hydrodynamic forces from flow parameters, using velocity and/or its time or spatial derivative (Moreau

† Email address for correspondence: juan.li@kcl.ac.uk

1952; Lin & Rockwell 1996; Noca 1996; Noca *et al.* 1997; Zhu *et al.* 2002, 2007). These approaches are usually derived based on the algebraic Bernoulli equation (Xia & Mohseni 2013), the unsteady Blasius equation (Milne-Thomson 1960; Streitlien & Triantafyllou 1995; Ford & Babinsky 2013) and the moment-equation based integral formulae (Saffman 1995; Howe 1995). Except for these theoretical force approaches, there have been many experimental and computational studies verifying and utilizing the aforementioned methods, examples including experimental works such as Norberg (2003); Birch & Dickinson (2003); Shew *et al.* (2006) and computational works from Ploumhans *et al.* (2002); Hsieh *et al.* (2010). However, there has not been much in way of theoretical updates on these works.

Recently, Li & Wu (2018) proposed and adopted (Li *et al.* 2021) the vortex force map method to extract force from the velocity and vorticity fields, making use of the integral force formula by Howe (1995). In this approach, forces acting on a body are expressed as a scalar product between the velocity, the vortex force vector, and the local vortex strength. The vortex force maps, constructed in order to identify the force contribution effect of each vortex in the flow field, are dependent on the body geometry only and not on flow features. Moreover, the map provides a visual display of the force-producing and reducing critical regions and directions. An extension to three-dimensional flows with application to a delta wing was later demonstrated by Li *et al.* (2020*b*) and the extension to the moment on a airfoil was demonstrated by Li *et al.* (2020*a*). This was followed by the treatment of low Reynolds number flows in Li *et al.* (2021), extending the vortex force map method to more general cases for a wider range of Reynolds numbers (from $O(10)$ to $O(1e6)$) by adding the viscous-pressure force and skin friction force contributions to the total force. The formulation for vortex-pressure force maps were also updated so that vortices far away from the body have a vanishing effect on force, making it possible to identify the force contribution effect of each given vortex based solely on the near-field flow. To facilitate its application in extracting forces from PIV-like flow velocity and vorticity data, the dependence of accuracy on the resolution of the mesh used to compute the forces, as well as calculation/integration domain, were also investigated in that work. Note that, here, a mesh is used to demonstrate the PIV-like flow field where the velocity/vorticity field data are pre-provided for the force calculation, while in other cases like the vortex panel method, a mesh is no longer needed.

So far, the methods described above all consider flows around a single body, it has been less clear how flows involving multiple bodies can be treated by these methods. Bai *et al.* (2014) proposed the generalized Kutta-Joukowski force formula for two-dimensional inviscid flow involving multiple bound and free vortices, multiple airfoils, and vortex generation (vorticity production) by using a specific momentum approach. Chang *et al.* (2008) proposed a many-body force decomposition approach by employing auxiliary potential functions with applications to flow about multi-cylinders. However, Howe's original approach aimed at multi-body flows still needs further exploration since its application in airfoil or wing aerodynamics is not complete. Moreover, the Chang *et al.* (2008) theory does not lend itself to a visual representation of the individual force contributions to each body from the vorticity distribution in the flow field. Therefore in this work, the vortex force map method is extended to multi-body flows by deriving the vortex force formula for each individual body in a multi-body setup. Similar to the previous work, we break down the contribution into three effects: the vortex-pressure force caused by free vorticity in the flow field, the viscous-pressure force, and the skin friction force caused by vorticity on the body surface. We aim to develop individual vortex-pressure force maps for each body in the presence of other bodies. To demonstrate its application, this method is used to study impulsively started flows around wing-

flap configurations and validate the results against computational fluid dynamics (CFD) results. Subsequently, we will also use the method to study the force oscillation behavior related to the vortex flow pattern.

In section 2, the derivation of the vortex force map approach for multi-body force decomposition is presented, with guidance on designing vortex-pressure force maps and applying the force approach in calculating total force. In section 3, vortex-pressure force map analysis for two-dimensional wing-flap configurations at different stages of deployment and at different angles of attack is demonstrated. Section 4 is dedicated to the application of the vortex force map approach to unsteady flows around the wing-flap configurations with different deflection angles of the flap, at different Reynolds numbers, and for different angles of attack. Theoretical results of force variation with time are validated against CFD. Concluding remarks are given in section 5.

2. Vortex force decomposition for multi-body flows

Consider viscous flows of constant density ρ and viscosity μ around a number of M solid bodies. Each body has a volume Ω_{mB} $(m = 1, 2, ..., M)$, bounded by a closed surface S_{mB} $(m = 1, 2, ..., M)$. (In the two-dimensional case, the bounding surface S_{mB} reduces to a closed curve l_{mB}). The control volume Ω is bounded by S_∞ at infinity. In this section we will derive the force $\overrightarrow{F_i}$ acting on the ith-body as reference, which can be decomposed into a normal component F_{iN} and an axial component F_{iA}, or a lift component L_i and a drag component D_i in the body-fixed frame (x, y, z) of the ith-body. Here, the free-stream velocity is V_∞ (incident at an angle α to the ith-body axis), the velocity of the flow field is $\overrightarrow{U}$, and the vorticity is $\overrightarrow{\omega}$. The problem setup and the schematic of the flow and the force components are shown in Figure 1. The flow is governed by the incompressible momentum equation in the Lamb-Gromyko form

$$\nabla\left(P + \frac{1}{2}\rho U^2\right) + \rho\overrightarrow{\omega} \times \overrightarrow{U} = -\rho\frac{\partial\overrightarrow{U}}{\partial t} - \mu\nabla \times \overrightarrow{\omega}, \tag{2.1}$$

and the incompressible continuity equation

$$\nabla \cdot \overrightarrow{U} = 0. \tag{2.2}$$

For each body (i), a set of hypothetical potentials ϕ_{ik} is introduced here for the derivation of force acting on the ith-body as a function of vorticity field, similar to that suggested by Howe (1995) for a single body case. Each ϕ_{ik} corresponds to the velocity potential for hypothetical potential fluid induced by the translational motion of Ω_{iB} at unit speed in the kth-direction (other bodies remain stationary for this purpose). According to the definition of the hypothetical potentials, they satisfy the Laplace equation in the entire field with boundary conditions blow

$$\begin{cases} \nabla^2\phi_i = 0 \\ \nabla\phi_{ik} \cdot \overrightarrow{n_{iB}} = -\overrightarrow{k} \cdot \overrightarrow{n_{iB}} = n_{iB,k}, \quad (x, y, z) \to S_{iB} \\ \nabla\phi_{ik} \cdot \overrightarrow{n_{mB}} = 0, \quad (x, y, z) \to S_{mB} \cup S_\infty \, (m \neq i) \end{cases}. \tag{2.3}$$

Here $\overrightarrow{n_{iB}}$ and $\overrightarrow{n_{mB}}$ are the normal vectors pointing inward from each body surface and $\overrightarrow{k}$ is the unit vector in kth-direction.

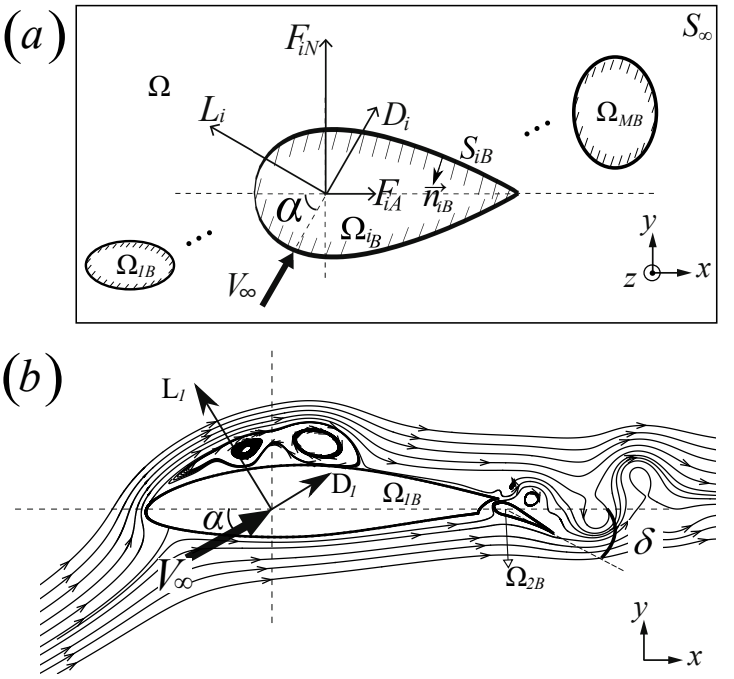

Figure 1: (a) A set of rigid bodies Ω_{mB} $(m = 1, 2, ..., M)$, bounded by S_{mB}, in translational outer flows with a control volume Ω bounded by S_∞ at infinity. The force acting on the *ith*-body may be either decomposed into a normal component (F_{iN}) and an axial component (F_{iA}), or a lift component (L_i) and a drag component (D_i). (b) Schematic display of vortex flow and various force components for a wing-flap configuration at arbitrary angle of attack (α) (x is along the chord line and y is perpendicular to the chord line). Here number of bodies $M = 2$, and $m = 1$ denotes the main airfoil, $m = 2$ denotes the flap.

2.1. *General vortex force expression for the ith-body in three dimensions*

According to the most commonly used force formula (Chang 1992), the force acting on the *ith*-body is comprised of the pressure force and the skin friction force,

$$\begin{cases} \overrightarrow{F_i} = \overrightarrow{F_i}^{(pressure)} + \overrightarrow{F_i}^{(friction)} \\ \overrightarrow{F_i}^{(pressure)} = \iint_{S_{iB}} P\overrightarrow{n_{iB}} dS \\ \overrightarrow{F_i}^{(friction)} = \mu \iint_{S_{iB}} \overrightarrow{n_{iB}} \times \overrightarrow{\omega} dS \end{cases} \tag{2.4}$$

among which the pressure force can be transformed into a function of the vorticity field by using the Lamb-Gromyko equation (2.1) and the boundary condition (2.3) satisfied on the body surface.

Integrating the scalar product of $\nabla\phi_{ik}$ and equation (2.1) on the control volume, (i.e. $\iiint_\Omega \nabla\phi_{ik} \bullet (2.1) d\Omega$), with the help of the incompressible continuity equation (2.2) and the identities $\psi\nabla \bullet \overrightarrow{G} \equiv \nabla \bullet \left(\psi\overrightarrow{G}\right) - \nabla\psi \bullet \overrightarrow{G}$ and $\nabla \bullet \left(\nabla \times \overrightarrow{G}\right) \equiv 0$ (ψ denotes an arbitrary scalar and $\overrightarrow{G}$ an arbitrary tensor), we have

$$\iiint_{\Omega} \nabla \bullet (P\nabla\phi_{ik})\, d\Omega = -\rho \iiint_{\Omega} \nabla \bullet \left(\phi_{ik}\frac{\partial \overrightarrow{U}}{\partial t}\right) d\Omega - \rho \iiint_{\Omega} \nabla\phi_{ik} \bullet \left(\overrightarrow{\omega} \times \overrightarrow{U}\right) d\Omega$$
$$-\mu \iiint_{\Omega} \nabla \bullet \left(\phi_{ik} \nabla \times \overrightarrow{\omega}\right) d\Omega$$

Applying Green's theorem to transform the volume integral in the above equation into the surface integral, and with application of identity $\phi_{ik}\nabla\times\overrightarrow{\omega} = \nabla\times\left(\phi_{ik}\overrightarrow{\omega}\right) + \overrightarrow{\omega}\times\nabla\phi_{ik}$ and $\iint_S \nabla\times\overrightarrow{G}\bullet\overrightarrow{n}\,dS = 0$ on any enclosed surfaces, we have

$$\begin{aligned} -\iint_{\sum_{m=1}^{M} S_{mB}+S_{\infty}} P\nabla\phi_{ik}\cdot\overrightarrow{n_{mB}}dS = &-\rho \iint_{\sum_{m=1}^{M} S_{mB}+S_{\infty}} \phi_{ik}\frac{\partial\overrightarrow{U}}{\partial t}\bullet\overrightarrow{n}\,dS \\ &-\rho\iiint_{\Omega}\nabla\phi_{ik}\bullet\left(\overrightarrow{\omega}\times\overrightarrow{U}\right)d\Omega \\ &-\mu\iint_{\sum_{m=1}^{M} S_{mB}+S_{\infty}} \overrightarrow{\omega}\times\nabla\phi_{ik}\bullet\overrightarrow{n}\,dS \end{aligned} \quad (2.5)$$

Substituting equation (2.3) into the LHS of equation (2.5), we have

$$-\iint_{\sum_{m=1}^{M} S_{mB}+S_{\infty}} P\nabla\phi_{ik}\cdot\overrightarrow{n_{mB}}dS = \iint_{S_{iB}} Pn_{iB,k}dS. \quad (2.6)$$

As the flow at infinity is undisturbed and irrotational, we have

$$\begin{cases} \rho\iint_{S_{\infty}}\phi_{ik}\frac{\partial\overrightarrow{U}}{\partial t}\bullet\overrightarrow{n}\,dS = 0 \\ \mu\iint_{S_{\infty}}\overrightarrow{\omega}\times\nabla\phi_{ik}\bullet\overrightarrow{n}\,dS = 0 \end{cases}. \quad (2.7)$$

Projecting the force equation (2.4) into the *kth*-direction and substituting equations (2.5)-(2.7) into it, we arrive at the force formula in the form of a summation of four components: the added mass force $F_{ik}^{(Add)}$, the vortex pressure force $F_{ik}^{(vor-P)}$, the viscous pressure force $F_{ik}^{(vis-P)}$ and the skin-friction force $F_{ik}^{(friction)}$, and the first three make up the pressure force $F_{ik}^{(pressure)}$.

$$\begin{cases} F_{ik} = \underbrace{F_{ik}^{(Add)} + F_{ik}^{(vor-P)} + F_{ik}^{(vis-P)}}_{F_{ik}^{(pressure)}} + F_{ik}^{(friction)} \\ F_{ik}^{(Add)} = -\rho\iint_{\sum_{m=1}^{M} S_{mB}}\phi_{ik}\frac{\partial\overrightarrow{U}}{\partial t}\bullet\overrightarrow{n}\,dS \\ F_{ik}^{(vor-P)} = -\rho\iiint_{\Omega}\nabla\phi_{ik}\bullet\left(\overrightarrow{\omega}\times\overrightarrow{U}\right)d\Omega \\ F_{ik}^{(vis-P)} = -\mu\iint_{\sum_{m=1}^{M} S_{mB}}\overrightarrow{\omega}\times\nabla\phi_{ik}\bullet\overrightarrow{n_{iB}}dS \\ F_{ik}^{(friction)} = \mu\iint_{S_{iB}}\overrightarrow{n_B}\times\overrightarrow{\omega}\bullet\overrightarrow{k}\,dS \end{cases} \quad (2.8)$$

Some discussions on the force formula:

i) It is capable of any unsteady flows. For the first term (the added mass force) $F_{ik}^{(Add)}$, time is included explicitly by $\partial\overrightarrow{U}/\partial t$. While for the remaining terms, time is included implicitly by the time-dependent flow field data $\overrightarrow{\omega}$ and $\overrightarrow{U}$.

ii) The added mass force $F_{ik}^{(Add)}$, proportional to $\partial\overrightarrow{U}/\partial t$ on the body surface, is caused by acceleration, pitching, heaving and deformation of the body. Sometimes it is omitted

as studies have shown that the forces are dominated by the vortex forces for massively separated flow problems (Ansari *et al.* 2006; Xia & Mohseni 2013).

iii) As will be shown in section 4, the vortex-pressure force $F_{ik}^{(vor-P)}$ is the dominant force. According to the definition of hypothetical potential (2.3), $\nabla\phi_{ik} = 0$ at infinity, which ensures the above formula to be consistent with the fact that only near-body vortices are more likely to cause pressure variation while vortices far away from the body have negligible effects on force.

iv) The viscous-pressure force $F_{ik}^{(vis-P)}$ and the skin-friction force $F_{ik}^{(friction)}$ contain the integration of vorticity $\overrightarrow{\omega}$ on the body surface. In practice, we interpolate the vorticity in the boundary layer to the body surface as an approximation.

v) The vortex torque decomposition method for multi-bodies is outlined in appendix A and will be further studied in the future.

2.2. *General vortex force expression for the ith-body in two dimensions*

In two-dimensional flow, we have $\nabla = \left(\frac{\partial}{\partial x}, \frac{\partial}{\partial y}, 0\right)$, $\overrightarrow{\omega} = (0, 0, \omega_z)$, and $\overrightarrow{U} = (u, v, 0)$. The force expression (2.8) can now be simplified into

$$\begin{cases} F_{ik} = \underbrace{F_{ik}^{(Add)} + F_{ik}^{(vor-P)} + F_{ik}^{(vis-P)}}_{F_{ik}^{(pressure)}} + F_{ik}^{(friction)} \\ F_{ik}^{(Add)} = -\rho \iint_{\sum_{m=1}^{M} l_{mB}} \phi_{ik} \frac{\partial \overrightarrow{U}}{\partial t} \bullet \overrightarrow{n}\, dl \\ F_{ik}^{(vor-P)} = \rho \iint_{\Omega} \overrightarrow{\Lambda}_{ik} \bullet \overrightarrow{U} \omega_z d\Omega \\ F_{ik}^{(vis-P)} = \mu \oint_{\sum_{m=1}^{M} l_{mB}} \omega_z d\phi_{ik} \\ F_{i}^{(friction)} = \mu \oint_{l_{iB}} \omega_z \overrightarrow{k} \bullet \overrightarrow{dl} \end{cases} \tag{2.9}$$

where $\overrightarrow{U} = (u, v)$ is the vortex velocity *in the ith body-fixed frame*. The integral in vortex-pressure force term is defined within the whole fluid region Ω, and the viscous-pressure and skin-friction terms along the body surface l_{mB} $(m = 1, 2, ...M)$. The vortex-pressure force factor is expressed as

$$\overrightarrow{\Lambda}_{ik} = \left(\frac{\partial \phi_{ik}}{\partial y}, -\frac{\partial \phi_{ik}}{\partial x}\right). \tag{2.10}$$

where ϕ_{ik} is defined in (2.3).

2.3. *Vortex lift and drag expression for the ith-body in two dimensions*

Consider in the *ith*-body-fixed frame, the free stream velocity is $\overrightarrow{V_\infty}$ with an incident angle of α. The lift expression for the *ith*-body can be given by choosing the direction $\overrightarrow{k} = \overrightarrow{k_L} = (-\sin\alpha, \cos\alpha)$ in expression (2.9)

$$\begin{cases} L_i = \underbrace{L_i^{(Add)} + L_i^{(vor-P)} + L_i^{(vis-P)}}_{L_i^{(pressure)}} + L_i^{(friction)} \\ L_i^{(Add)} = -\rho \iint_{\sum_{m=1}^{M} l_{mB}} \phi_{iL} \frac{\partial \overrightarrow{U}}{\partial t} \bullet \overrightarrow{n}\, dl \\ L_i^{(vor-P)} = \rho \iint_{\Omega} \overrightarrow{\Lambda}_{iL} \bullet \overrightarrow{U} \omega_z d\Omega \\ L_i^{(vis-P)} = \mu \oint_{\sum_{m=1}^{M} l_{mB}} \omega_z d\phi_{iL} \\ L_i^{(friction)} = \mu \oint_{l_{iB}} \omega_z \overrightarrow{k_L} \bullet \overrightarrow{dl} \end{cases} . \tag{2.11}$$

Similarly, the drag expression for the *ith*-body can be given by choosing the direction $\overrightarrow{k} = \overrightarrow{k_D} = (\cos\alpha, \sin\alpha)$ in expression (2.9)

$$\begin{cases} D_i = \underbrace{D_i^{(Add)} + D_i^{(vor-P)} + D_i^{(vis-P)}}_{D_i^{(pressure)}} + D_i^{(friction)} \\ D_i^{(Add)} = -\rho \iint_{\sum_{m=1}^{M} l_{mB}} \phi_{iD} \frac{\partial \overrightarrow{U}}{\partial t} \bullet \overrightarrow{n} dl \\ D_i^{(vor-P)} = \rho \iint_{\Omega} \overrightarrow{\Lambda}_{iD} \bullet \overrightarrow{U} \omega_z d\Omega \\ D_i^{(vis-P)} = \mu \oint_{\sum_{m=1}^{M} l_{mB}} \omega_z d\phi_{iD} \\ D_i^{(friction)} = \mu \oint_{l_{iB}} \omega_z \overrightarrow{k_D} \bullet \overrightarrow{dl} \end{cases} . \tag{2.12}$$

Here the vortex-pressure force vector

$$\overrightarrow{\Lambda_{iL}} = (\frac{\partial \phi_{iL}}{\partial y}, -\frac{\partial \phi_{iL}}{\partial x}) \tag{2.13}$$

is for lift, and

$$\overrightarrow{\Lambda}_{iD} = (\frac{\partial \phi_{iD}}{\partial y}, -\frac{\partial \phi_{iD}}{\partial x}) \tag{2.14}$$

is for drag. The hypothetical potentials ϕ_{iL} and ϕ_{iD} are induced by the translational movement of the *ith*-body in the $\overrightarrow{k_L} = (-\sin\alpha, \cos\alpha)$ and $\overrightarrow{k_D} = (\cos\alpha, \sin\alpha)$ direction with unit velocity, respectively, i.e.

$$\begin{cases} \frac{\partial^2 \phi_{iL}}{\partial x^2} + \frac{\partial^2 \phi_{iL}}{\partial y^2} = 0 \\ \frac{\partial \phi_{iL}}{\partial n} = \overrightarrow{n} \cdot (-\sin\alpha, \cos\alpha) \qquad (x,y) \to l_{iB} \\ \frac{\partial \phi_{iL}}{\partial x} = \frac{\partial \phi_{iL}}{\partial y} = 0 \qquad (x,y) \to l_{mB}\,(m \neq i) \ \cup S_\infty \end{cases} \tag{2.15}$$

$$\begin{cases} \frac{\partial^2 \phi_{iD}}{\partial x^2} + \frac{\partial^2 \phi_{iD}}{\partial y^2} = 0 \\ \frac{\partial \phi_{iD}}{\partial n} = \overrightarrow{n} \cdot (\cos\alpha, \sin\alpha) \qquad (x,y) \to l_{iB} \\ \frac{\partial \phi_{iD}}{\partial x} = \frac{\partial \phi_{iD}}{\partial y} = 0 \qquad (x,y) \to l_{mB}\,(m \neq i) \ \cup S_\infty \end{cases} \tag{2.16}$$

Thus, to obtain the vortex force factors $\overrightarrow{\Lambda}_{iL}$ and $\overrightarrow{\Lambda}_{iD}$, one simply needs to solve the Laplace models (2.15) and (2.16).

2.4. *Method to plot vortex-pressure force maps and calculate total force*

Expressions (2.11) and (2.12) give the force as the function of the vorticity field, in which the free vorticity in the flow field contributes to the pressure force and the vorticity on the body surface contributes to both pressure force and skin-friction force. As will be discussed later, the dominant force component is vortex-pressure force, in the form of the integration of a scalar product between the vortex-pressure force vectors defined in (2.13) and (2.14) and the local velocity. The vortex-pressure force vectors are function of position but independent of the flow field (incl. Reynolds number) and only dependent on the body shape and the angle of attack. Thus the vortex-pressure force vectors can be precomputed without knowing the flow field by solving equations (2.15) and (2.16) numerically. More details will be given in the next section.

On the one hand, these vectors can be used to build vortex-pressure force maps which can help analyze force oscillating behavior with relation to the vortex flow pattern and

identify the critical regions and directions for positive and negative force production by a given vortex.

On the other hand, they can be used together with force formulas (2.11) and (2.12) to obtain total forces if the properties of vortices (velocity and circulation) in the flow field and on the body surface are obtained through analytical, numerical or experimental methods.

a) *Vortex-pressure force map analysis*

Vortex force maps in the two-dimensional plane (x, y) for the ith-body are designed based on the precomputed vortex-pressure force vectors $\overrightarrow{\Lambda}_{iL}$ for lift force and $\overrightarrow{\Lambda}_{iD}$ for drag given by (2.13) and (2.14). Each map contains force lines that are locally parallel to the vortex force vectors, which can be obtained through a streamline procedure, with the velocity replaced by the vortex force factors. It also contains contours of $\left|\overrightarrow{\Lambda}_{iL}\right|$ or $\left|\overrightarrow{\Lambda}_{iD}\right|$. Vortex force map is defined in such a way that the force contribution of any individual vortex can be easily identified according to its circulation (sign and magnitude), position and direction (the angle between the vortex force line and streamline at the point of the vortex). Thus lift-increasing or drag-reducing directions and critical regions of a given vortex for each body can be defined in a similar way as in Li & Wu (2018).

b) *Calculation of total force*

With vortex force vectors precomputed for the ith-body, once velocity field $\overrightarrow{U}$ and vorticity field ω_z can be computed or measured, total forces can then be directly obtained from the vortex force formulas . This can be done as follows.

Given geometry and position of M bodies, the lift and drag force vectors of the ith-body at an angle of attack α can be given by finding the solution of hypothetical potentials ϕ_{iL} and ϕ_{iD} for the Laplace equations (2.15) and (2.16). The hypothetical potentials ϕ_{iL} and ϕ_{iD} are then substituted into expressions (2.13) and (2.14) to give the vortex force vectors $\overrightarrow{\Lambda}_{iL}$ and $\overrightarrow{\Lambda}_{iD}$. It is clear that for multibody setups with relative motion, the hypothetical potential will need to be updated at each point in time. However in reality, the variation of the hypothetical potential with relative position is smooth as long as there is no contact between the bodies. It is easy to interpolate between different precomputed relative positions to improve computational efficiency. In addition, the maps can be computed using a potential-type method at a very low computational cost.

i) For the vortex-pressure force, substitute $\overrightarrow{\Lambda}_{iL}$ and $\overrightarrow{\Lambda}_{iD}$ into the first terms of (2.11) and (2.12) to calculate vortex-pressure lift $L_i^{(vor-P)}$ and drag $D_i^{(vor-P)}$.

ii) For the viscous-pressure force, substitute ϕ_{iL} and ϕ_{iD} into the second terms of (2.11) and (2.12) obtain the viscous-pressure lift $L_i^{(vis-P)}$ and drag $D_i^{(vis-P)}$.

iii) For the skin-friction force, we use the third term in (2.11) and (2.12) to compute skin-friction lift $L_i^{(friction)}$ and drag $D_i^{(friction)}$.

3. Vortex-pressure force map analysis for wing-flap configurations

In this section, three slotted wing-flaps with deflection angles of flap of -20^o, 0^o and 20^o are used to demonstrate the construction of the vortex-pressure force maps for a specific body among a series of bodies and to identify the force contribution effect of each given vortex to each body according to its position, strength and local velocity. Here we only consider lift and drag force maps, which depend on the geometry as well as angle of attack.

For a wing-flap model, with geometry (the main airfoil -Ω_{1B}, the flap -Ω_{2B}, and the deflection angle -δ) and angle of attack α given, the Laplace equations (2.15) and (2.16)

are solved by using the vortex panel method as suggested by Katz & Plotkin (2001) in solving the steady-state potential flow. The method solves the Laplace equation via a superposition of singularity elements on the body surface and enforcing non-penetration boundary condition on the surface and zero total circulation, which has been validated against that solved by the commercial code CFX in Li & Wu (2018) (using the Laplace Equation option for heat transfer). In this solver, the solution for the hypothetical potential is the non-circulatory one among the infinite number of possibilities in 2-dimensional flow. The vortex-pressure force vectors for lift ($\overrightarrow{\Lambda_{iL}}$, $i = 1, 2$) and for drag ($\overrightarrow{\Lambda_{iD}}$, $i = 1, 2$) are then computed by (2.13) and (2.14). With the vortex force factors precomputed, the vortex-pressure force maps are then generated following the steps in section 2.4.

Figures 2-5 show the vortex-pressure force maps for wing-flap configurations. In these maps, the vortex force lines are represented as solid arrows which are parallel to the local vortex force vectors ($\overrightarrow{\Lambda_{iL}}$ or $\overrightarrow{\Lambda_{iD}}$, $i = 1, 2$). The contour lines for the norm of vortex force vectors ($\left|\overrightarrow{\Lambda_{iL}}\right|$ or $\left|\overrightarrow{\Lambda_{iD}}\right|$, $i = 1, 2$) are also presented. According to the vortex-pressure force maps, a counter-clockwise rotating vortex (e.g. a trailing edge vortex (TEV) rolled up on the trailing edge (TE)) contributes positive force (lift or drag) if it moves so as to have a component of motion in the direction of the vortex force lines, while a clockwise rotating vortex (e.g. a leading edge vortex (LEV) formed on the leading edge (LE)) contributes positive force (lift or drag) if it moves so as to have a component of motion opposed to the vortex force lines, and vice versa.

3.1. *Influence of deflection angle of flap on vortex-pressure force maps*

Figure 2 shows the vortex-pressure force maps for both lift and drag of the main airfoil (Ω_{1B}) in the wing-flap configurations with different deflection angles of flap: $\delta = -20^o$, 0^o and 20^o. We can see that the norm of the vortex force vectors $\left|\overrightarrow{\Lambda_{1L}}\right|$ and $\left|\overrightarrow{\Lambda_{1D}}\right|$ for the main airfoil decrease with the distance from the wing-flap configuration, and the peak values locate in the LE area of the main airfoil, the connecting area of two bodies and the TE area of the flap. The vortex force lines near the flap rotate slowly with increasing the deflection angle of flap.

Figure 3 is the vortex-pressure force maps for the flap (Ω_{2B}) in the same wing-flap configurations. We can see that the norm of the vortex force vectors $\left|\overrightarrow{\Lambda_{2L}}\right|$ and $\left|\overrightarrow{\Lambda_{2D}}\right|$ for the flap decrease with the distance from the flap, and the peak values locate in the connecting area of two bodies and the TE area of the flap. The vortex force lines appear to rotate with increasing the deflection angle of flap.

3.2. *Influence of angle of attack on vortex-pressure force maps*

Figures 4 and 5 show the vortex-pressure force maps for both lift and drag of the main airfoil as well as the flap in a $\delta = 0^o$ wing-flap configuration at $\alpha = 45^o$ and $\alpha = 60^o$, respectively. Compared with those maps at $\alpha = 20^o$ in Figures 2 and 3 (c,d), we can see that the vortex-pressure force maps for different angles of attack look similar. We can also see from these maps that the larger the angle of attack is, the smaller the vortex lift factors are and the larger the vortex drag factors are in corresponding positions. Note that in the present vortex-pressure force maps, the fact that vorticity far-away from the body have negligible effect on force is satisfied automatically.

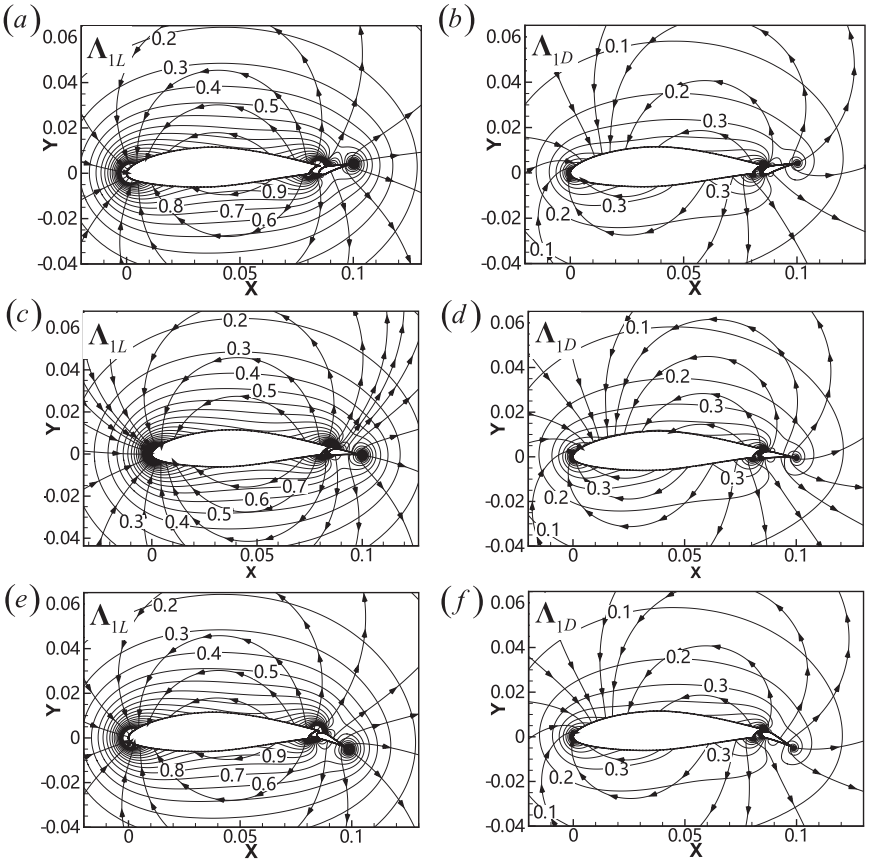

Figure 2: Vortex-pressure force maps for lift and for drag of the main airfoil at $\alpha = 20^o$ with different flap angles : (a),(c),(e) are for lift with flap angle $\delta = -20^o$, 0 and 20^o, respectively; (b),(d),(e) are for drag with the same flap angles. The lines with arrows are vortex-pressure force lines locally parallel to the vector $\overrightarrow{\Lambda_{1L}}$ and $\overrightarrow{\Lambda_{1D}}$, and the lines without arrows are contours of magnitude of $\overrightarrow{\Lambda_{1L}}$ and $\overrightarrow{\Lambda_{1D}}$.

4. Vortex lift and drag for viscous flows around impulsively started wing-flap configurations

In this section, the vortex force map method is applied to impulsively started wing-flap flows. Here, the total force will be given by (2.11) and (2.12), with the velocity and vorticity field provided by CFD. The theoretical lift and drag results will be compared with those obtained from integrating the body surface pressure and skin-friction given by CFD code. Here all the flow field is assumed to be laminar. The contribution of different force components, contributed either from free vorticity in the flow field or from the vorticity on body surface, will be discussed. The force oscillation on the main airfoil as well as on the flap in relation to the evolution of the vortex structure in the flow field will be studied.

4.1. *Force approach and CFD method*

As discussed in section 2.4, the vortex force approach (2.11) and (2.12) can be used to calculate the total force acting on the body, with the vortex force factors precomputed by

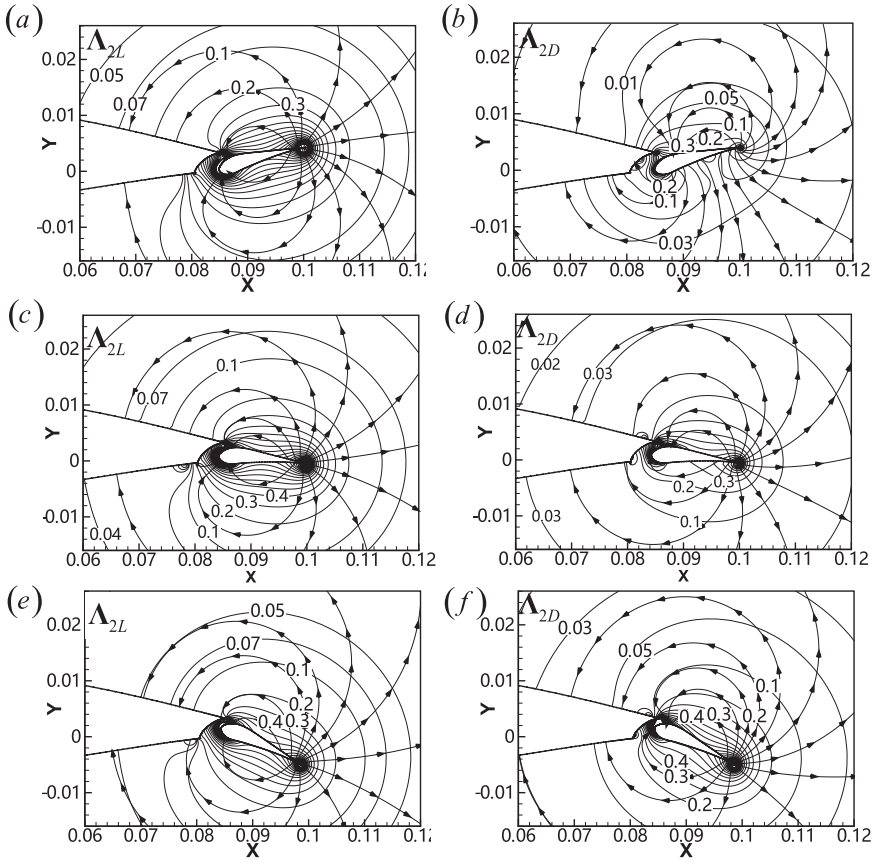

Figure 3: Vortex-pressure force maps for lift and for drag of the flap in the wing-flap configuration for $\alpha = 20^o$ with different flap angles : (a),(c),(e) are for lift with flap angle $\delta = -20^o$, 0 and 20^o, respectively; (b),(d),(e) are for drag with the same flap angles. The lines with arrows are vortex-pressure force lines locally parallel to the vector $\overrightarrow{\Lambda_{2L}}$ and $\overrightarrow{\Lambda_{2D}}$, and the lines without arrows are contours of magnitude of $\overrightarrow{\Lambda_{2L}}$ and $\overrightarrow{\Lambda_{2D}}$.

analytical or numerical methods, and the velocity and vorticity field given by conventional methods including a vortex panel method, CFD simulation or experimental measurement. The results of pressure lift $L_i^{(pressure)}$ and drag $D_i^{(pressure)}$ will be compared to the pressure lift and drag obtained by the integration of the body surface pressure in the CFD code, while the results of skin friction force $L_i^{(friction)}$ and $D_i^{(friction)}$ will be compared to the skin friction lift and drag obtained from the CFD code. Note that for the starting flow problem considered here, the added mass force $L_i^{(Add)}$ and drag $D_i^{(Add)}$ in equations (2.11) and (2.12) are infinite at the initial moment, and are 0 at any moment after the starting procedure.

Here, the force results will be represented in the form of nondimensional coefficients. The lift coefficient and drag coefficient are defined as

$$C_L = \frac{L}{\frac{1}{2}\rho V_\infty^2 c_A}, C_D = \frac{D}{\frac{1}{2}\rho V_\infty^2 c_A} \tag{4.1}$$

where c_A is the total chord length of the wing-flap configuration. The Reynolds number

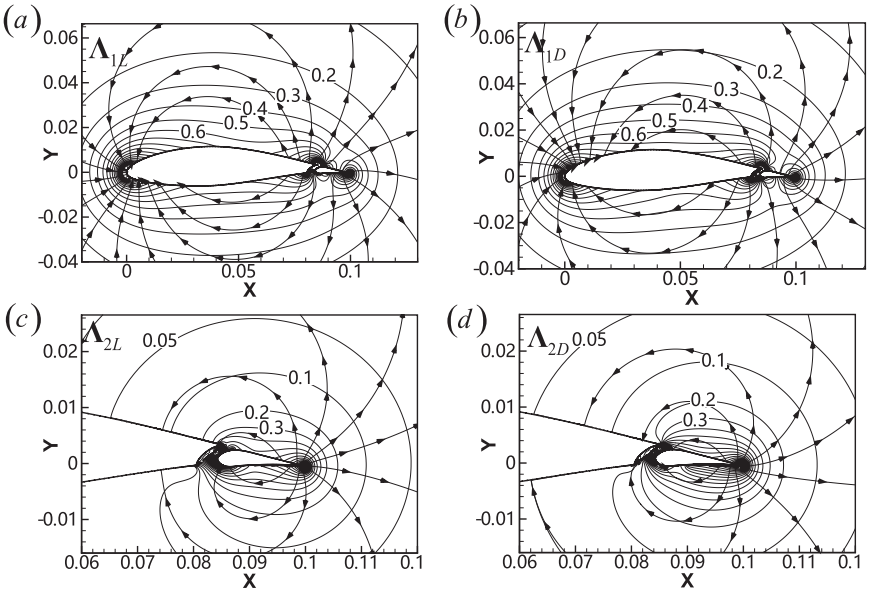

Figure 4: Vortex-pressure force maps for lift and for drag of the wing-flap configuration at $\alpha = 45^o$ with zero deflection angle of flap: (a) for lift of the main airfoil,(b) for drag of the main airfoil,(c) for lift of the flap; (d) for drag of the flap. The lines with arrows are vortex-pressure force lines locally parallel to the vector $\overrightarrow{\Lambda_{iL}}$ and $\overrightarrow{\Lambda_{iD}}$, and the lines without arrows are contours of magnitude of $\overrightarrow{\Lambda_{iL}}$ and $\overrightarrow{\Lambda_{iD}}$, where $i = 1, 2$, respectively.

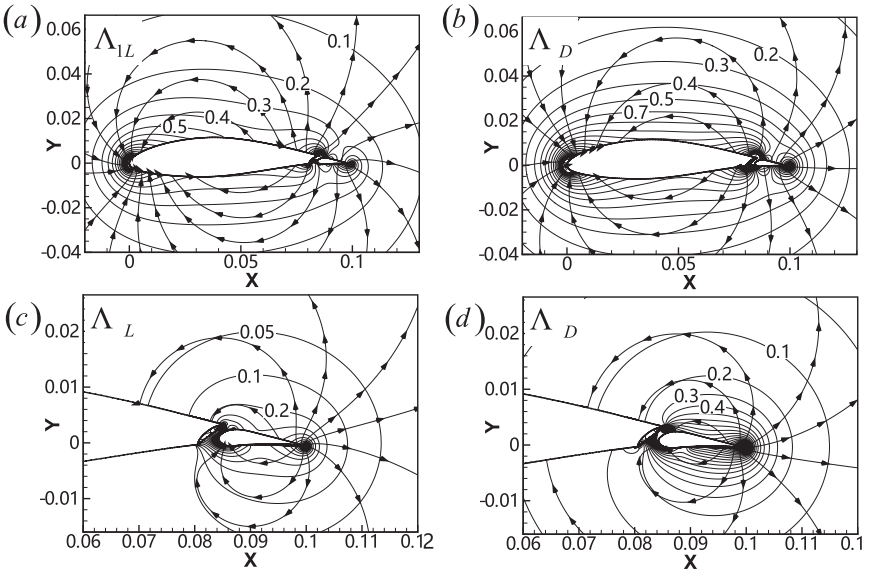

Figure 5: Vortex-pressure force maps for lift and for drag of the wing-flap configuration at $\alpha = 60^o$ with zero deflection angle of flap: (a) for lift of the main airfoil,(b) for drag of the main airfoil,(c) for lift of the flap; (d) for drag of the flap. The lines with arrows are vortex-pressure force lines locally parallel to the vector $\overrightarrow{\Lambda_{iL}}$ and $\overrightarrow{\Lambda_{iD}}$, and the lines without arrows are contours of magnitude of $\overrightarrow{\Lambda_{iL}}$ and $\overrightarrow{\Lambda_{iD}}$, where $i = 1, 2$, respectively.

in this paper is defined based on the total chord length: $Re = \rho V_\infty c_A/\mu$. The time-dependent forces will be displayed as functions of the non-dimensional time $\tau = tV_\infty/c_A$.

In CFD, the Navier–Stokes equations for unsteady laminar flow are solved numerically using the same method as used by Li & Wu (2019b). We have used the commercial code Fluent with a second-order upwind SIMPLE (semi-implicit method for pressure-linked equations) pressure–velocity coupling method. The computational domain is $30 \times c_A$ in the horizontal direction and $20 \times c_A$ in the vertical direction. Different mesh sizes (from 178293 to 264313) with 320 grids on the body surface of Ω_{1B} and 160 grids on the body surface of Ω_{2B} are chosen, for Reynolds numbers from 1000 to 1×10^5. The grid size normal to the wall and in the boundary layer is fine enough for convergence. The flow is impulsively started at a speed of $5m/s$ from an initially uniform flow.

4.2. *Vortex lift and drag evolution validated against CFD results*

In this subsection, the present vortex force method is applied to wing-flap configurations. Firstly, the flow at different Reynolds numbers will be studied. Then the effect of the angle of attack on the body force will be analyzed. Lastly, the results for different deflection angles of the flap will be demonstrated. All the results will be validated against CFD.

4.2.1. *Vortex lift and drag for different Reynolds numbers*

Here we fix the flap deflection angle $\delta = 0^o$ and the angle of attack $\alpha = 20^o$ to study the influence of different Reynolds numbers 1000, 5000, $1e4$ and $1e5$ on the body force decomposition. As shown in Figures 6(a-h), both pressure and friction component in lift for the main airfoil as well as for the flap calculated from the current approach agree well with CFD at different Reynolds numbers. Good agreements are also found in drag (Figures 7(a-h)).

The pressure forces (lift and drag) for both the main airfoil and the flap are singular at the initial moment, as the added mass force term in the pressure force is infinite as discussed above, and the vortex-pressure force term is also infinite due to an abrupt change in the body-surface vorticity. When Reynolds number is low (say $Re = 1000$), the force curves show periodic oscillation at large time ($\tau \geqslant 8$). When the Reynolds number is large enough ($Re \geqslant 1e4$), the friction forces are close to 0 and the pressure forces show some small amplitude oscillation related to the generation and movement of small vortices.

4.2.2. *Vortex lift and drag for different deflection angles of flap*

Good comparison are also found between theory and CFD for wing-flap configurations with $\delta = \pm 20^o$ for fixed angle of attack $\alpha = 20^o$ and Reynolds number $Re = 1e4$, as shown in Figure 8 for lift and Figure 9 for drag. It can be seen that the pressure force, summation of the forces contributed by free vortex in the flow field (the vortex-pressure force) and the vorticity on the body surface (the viscous-pressure force), is the dominant force. Whereas the friction forces are minor. The pressure forces (both lift and drag) for $\delta = 20^o$ are significantly larger than those for $\delta = -20^o$.

4.2.3. *Vortex lift and drag for different angles of attack*

To demonstrate the validity of the proposed vortex force method for different angles of attack, the comparisons between theory and CFD results for a wing-flap configuration with $\delta = 0^o$ and for $Re = 1000$ at $\alpha = 45^o$ and 60^o are shown in Figure 10 for lift and in Figure 11 for drag. The comparisons agree well. The force curves show periodicity in these cases, and the period length for the main airfoil and the flap are equal at the same

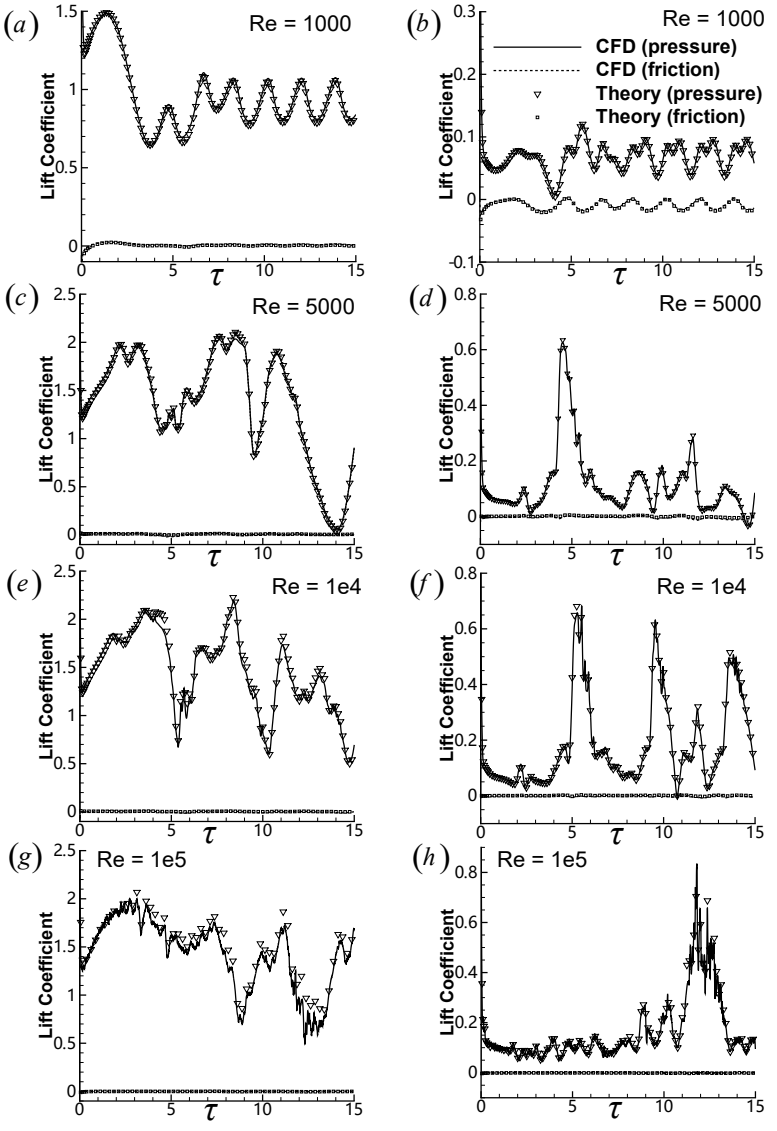

Figure 6: Comparison between theory and CFD for time-dependent lift coefficients for wing-flap configuration with deflection angle of flap $\delta = 0^o$ for $\alpha = 20^o$ at $Re = 1000, 5000, 1e4$ and $1e5$. (a),(c),(e) and (g) are for the main airfoil; (b),(d),(f) and (h) are for the flap.

angle of attack. The force oscillating behavior related to the vortex evolution in the flow field will be discussed in section 4.3.

4.3. *Vortex force analysis*

In this subsection, the evolution of three force components (the vortex-pressure force, the viscous-pressure force, and the skin-friction force) acting on both main airfoil and flap are studied. The relationship between the variation of dominant force (the vortex-pressure force) against time and the change of vortex flow structures is analyzed. The example case of lift forces acting on a impulsively started wing-flap configuration with

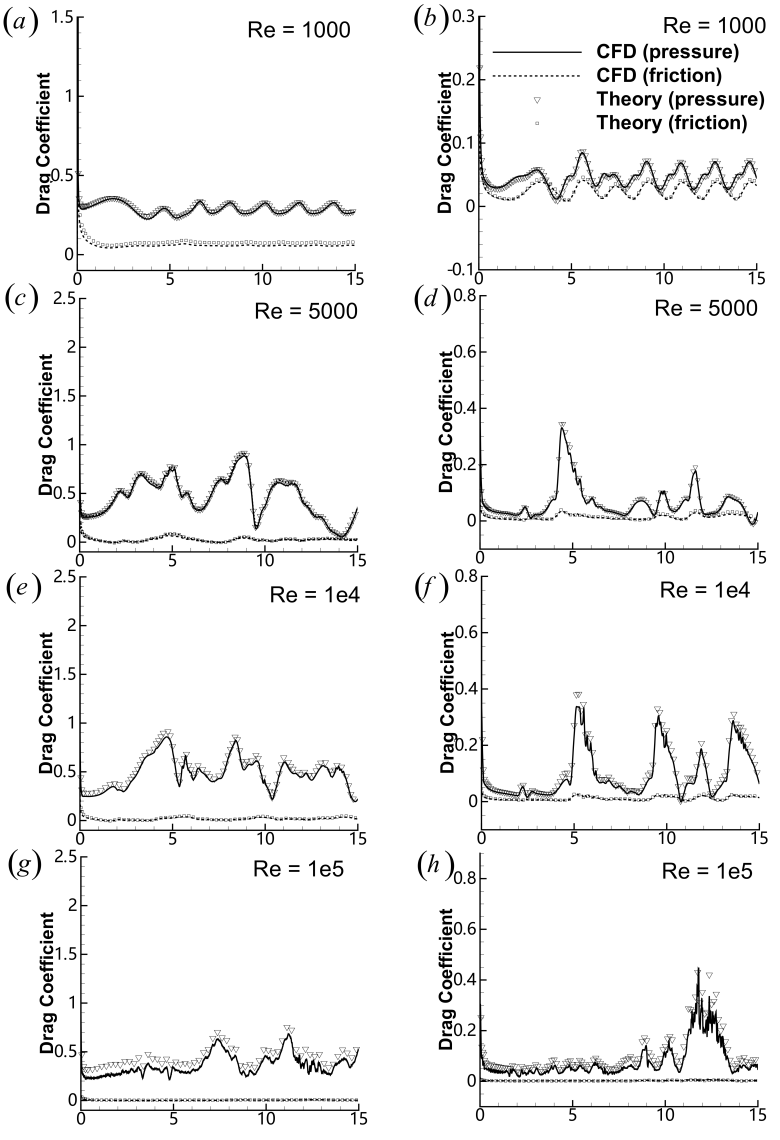

Figure 7: Comparison between theory and CFD for time-dependent drag coefficients for wing-flap configuration with deflection angle of flap $\delta = 0^o$ for $\alpha = 20^o$ at $Re = 1000, 5000, 1e4$ and $1e5$. (a),(c),(e) and (g) are for the main airfoil; (b),(d),(f) and (h) are for the flap.

$\delta = 0^o$ at $\alpha = 45^o$, $Re = 1000$ are presented here. The lift and drag results for other cases, at different angles of attack, different Reynolds numbers, and with different deflection angles, can be analyzed in a similar way.

4.3.1. *Analysis of different force components*

The evolution of the total lift coefficients and their three components for both the main airfoil and the flap in a wing-flap configuration is shown in Figure 12, together with the vorticity field and streamlines at typical instants: $\tau_0 = 0.125$, $\tau_i = i$ $(i = 1, 2, ..., 8)$. It can be seen from the figure that for both the main airfoil and the flap, the oscillating behavior

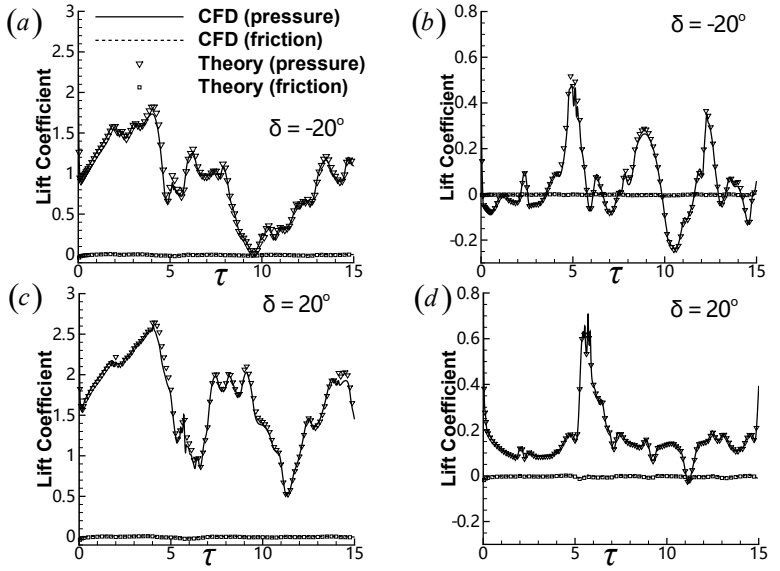

Figure 8: Comparison between theory and CFD for time-dependent lift coefficients for wing-flap configuration with deflection angle of flap $\delta = \pm 20^o$ for $\alpha = 20^o$ at $Re = 1e4$. (a),(c) are for the main airfoil; (b),(d) are for the flap.

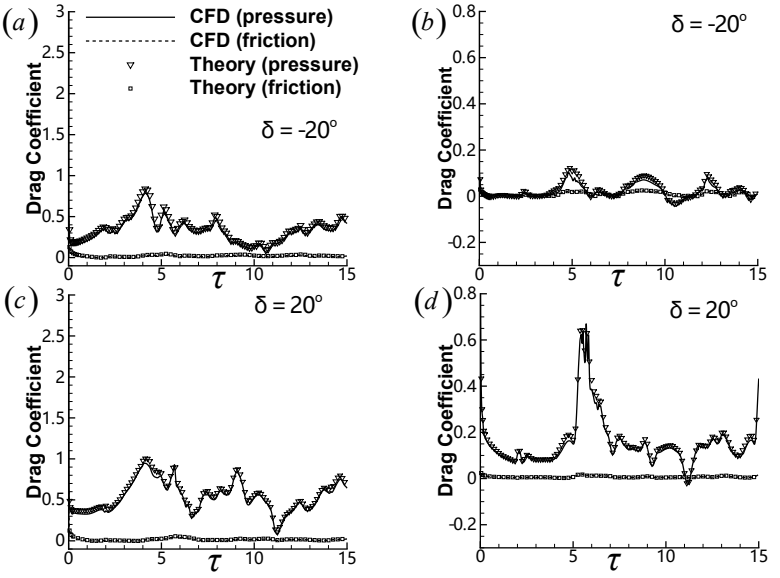

Figure 9: Comparison between theory and CFD for time-dependent drag coefficients for wing-flap configuration with deflection angles of flap $\delta = \pm 20^o$ for $\alpha = 20^o$ at $Re = 1e4$. (a),(c) are for the main airfoil; (b),(d) are for the flap.

of total lift coefficients is almost the same as those of vortex-pressure lift. Moreover, the summation of the viscous-pressure lift and the skin-friction lift on the main airfoil is about 0.2, and the summation of those two lift components on the flap is close to zero. In other words, the dominant forces are the vortex pressure forces. The oscillatory force curves for

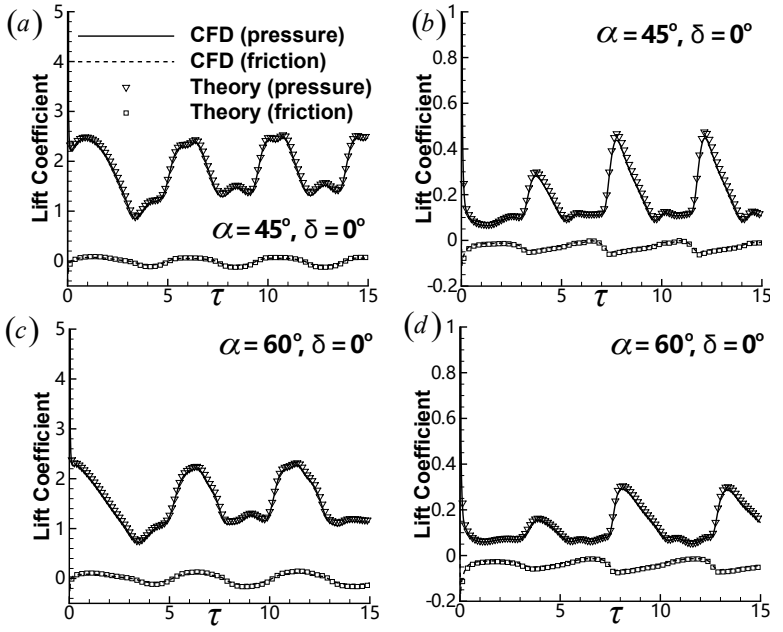

Figure 10: Comparison between theory and CFD for time-dependent lift coefficients for wing-flap configuration with 0^o deflection angles of flap at $Re = 1000$. (a) is for the main airfoil at $\alpha = 45^o$,(b) is for the flap at $\alpha = 45^o$; (c) is for the main airfoil at $\alpha = 60^o$,(d) is for the flap at $\alpha = 60^o$.

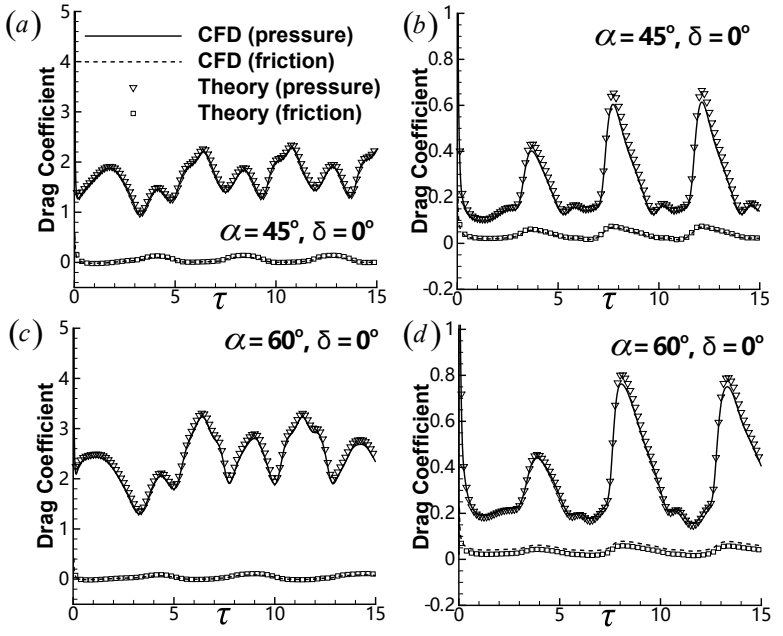

Figure 11: Comparison between theory and CFD for time-dependent drag coefficients for wing-flap configuration with 0^o deflection angles of flap at $Re = 1000$. (a) is for the main airfoil at $\alpha = 45^o$,(b) is for the flap at $\alpha = 45^o$; (c) is for the main airfoil at $\alpha = 60^o$,(d) is for the flap at $\alpha = 60^o$.

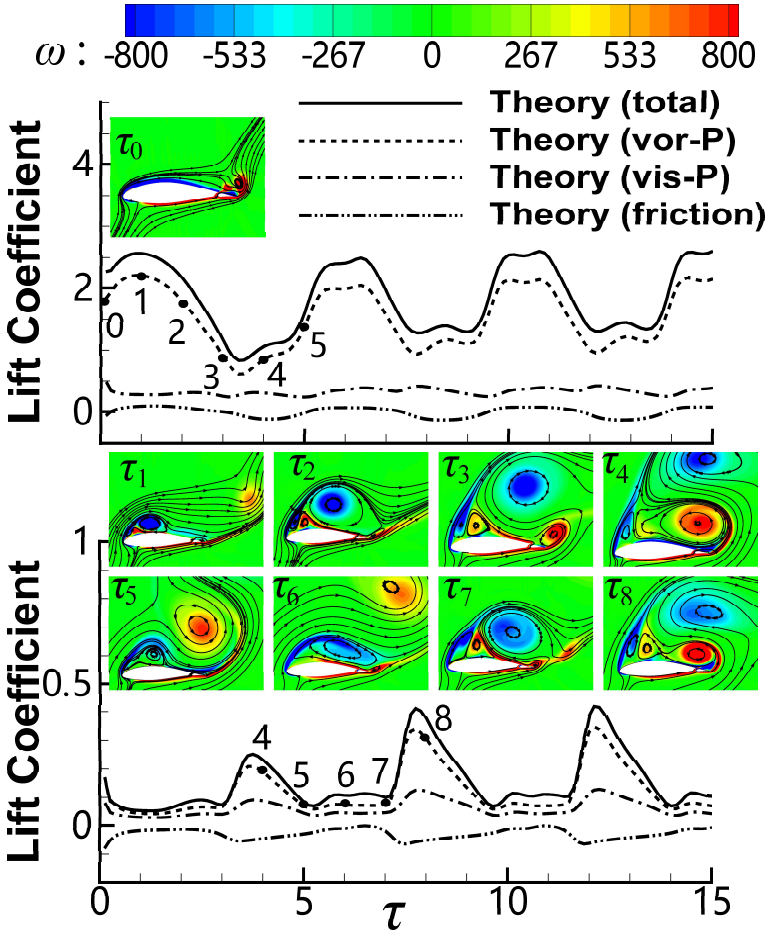

Figure 12: Vortex lift evolution for an impulsively started wing-flap configuration with 0^o deflection angles of flap for $\alpha = 45^o$ at $Re = 1000$. The curves on the top is for the main airfoil and on the bottom is for the flap. The total force as well as its three components are shown here. The vorticity distribution and streamlines at typical instants are also given.

all the components exhibit periodicity in the considering case, and the non-dimensional period is roughly equal to 4.

4.3.2. *Analysis of force oscillation related to vortex structures*

It can be seen from Figure 12 that the force variation has a close relationship with the evolution of vortex structure in the flow field, which is a reflection of the definition of

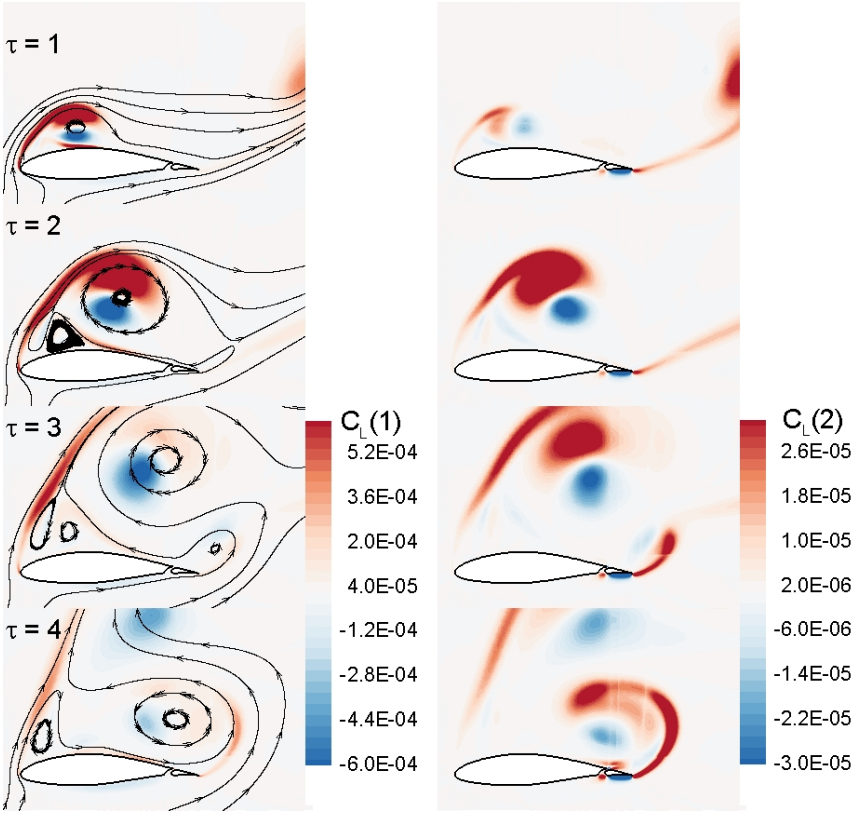

Figure 13: Contours of vortex lift distribution displaying lift coefficients acting on the main airfoil (left column) and on the flap (right column) contributed by local vortices, for a wing-flap configuration starting flow at instants $\tau = 1, 2, 3,$ and 4, with streamlines showing the vortex structure.

the dominant force (i.e. the vortex-pressure force): the integration of the scalar product of the local vortex force vector and velocity multiplied by vortex strength.

To demonstrate this relationship, we select one complete period of vortex-shedding. For the main airfoil, the lift experiences periodic oscillation with four stages: the LEV-augmentation stage; the high-level force plateau stage; the force drop stage; and the low-level force plateau stage. These four stages could be observed in Figure 12) (top). In the LEV-augmentation stage (from $\tau = 0$ to $\tau = 1$ and from $\tau = 4.5$ to $\tau = 5.5$), a clockwise LEV is expanding and convecting above the upper surface of the main airfoil. In the high-level force plateau stage (e.g. from $\tau = 5.5$ to $\tau = 6.5$), the earlier TEV moves downstream far from the body and a newly generated TEV is forming. In the force drop stage (from $\tau = 1$ to $\tau = 3$ and from $\tau = 6.5$ to $\tau = 7.5$), the main clockwise LEV and counterclockwise TEV are released and moving far away from the surface, in the meantime, a new pair of secondary LEV and a new TEV are developing at the leading edge and trailing edge respectively. In the low-level force plateau stage (from $\tau = 3$ to $\tau = 4.5$ and from $\tau = 7.5$ to $\tau = 9$), the secondary LEV pair and the newly formed TEV are expanding. These gradually occupy the whole area of the upper surface and interact with each other.

The spatial distribution of local vortex pressure lift due to the local vorticity at 8

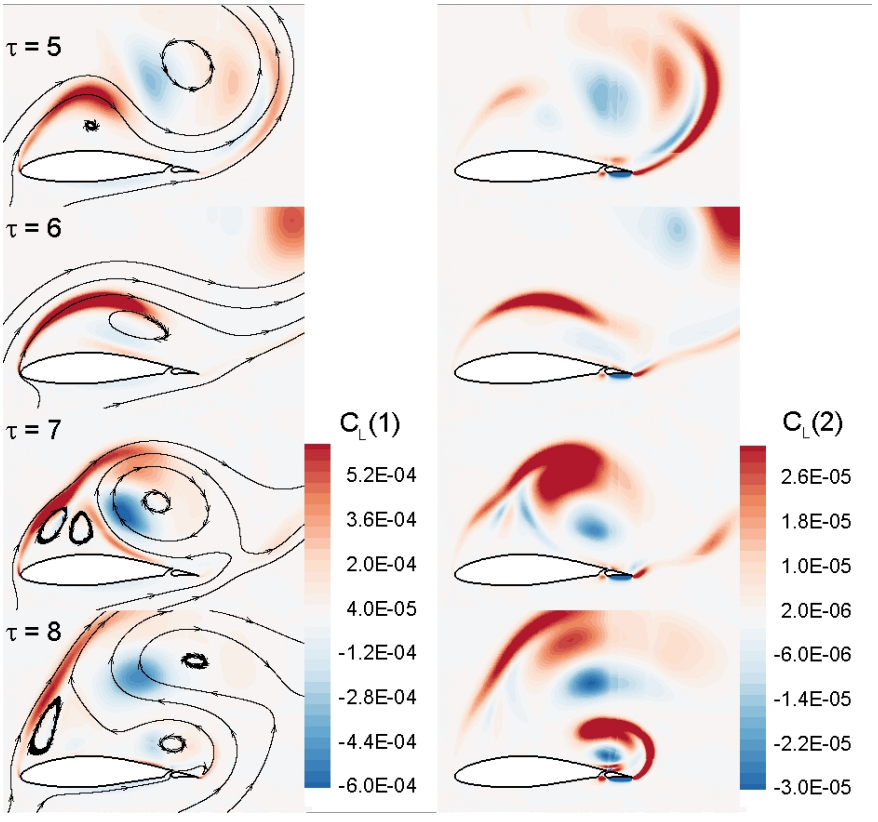

Figure 14: Contours of vortex lift distribution displaying lift coefficients acting on the main airfoil (left column) and on the flap (right column) contributed by local vortices, for a wing-flap configuration starting flow at instants $\tau = 5, 6, 7,$ and 8, with streamlines showing the vortex structure.

typical instants $\tau_i = i$ $(i = 1, 2, ..., 8)$ for the two bodies involved (the main airfoil and the flap) are shown in Figures 13 and 14. Figure 13 is for instants $\tau_i = i$ $(i = 1, 2, 3, 4)$ and figure 14 is instants $\tau_i = i$ $(i = 5, 6, 7, 8)$. The left columns in figures 13 and 14 are for the lift acting on the main airfoil and the right columns in the figures are for the lift acting on the flap. The theoretical vortex pressure lift coefficients on either the main airoil or the flap are obtained by summing the lift coefficients of vortices inside all grid cells. We can clearly see that the lift-contributing areas for both the main airfoil and the flap lie in an area close above the body surface. It can also be seen that there is an obvious relationship between the force variation and vortical flow structure.

Relating the left column of 13 and 14 to figure 12 allows us to analyze how the evolution of vortical structures in the flow field influence the lift acting on the main airfoil:

(i) The LEV-augmentation stage (e.g. from $\tau = 0$ to $\tau = 1$ and from $\tau = 4.5$ to $\tau = 5.5$) is caused by the growth of the main LEV above the upper surface of the main airfoil, resulting in a low-pressure suction ared above the leading edge.

(ii) The large force in the high-level force equilibrium stage (e.g. from $\tau = 5.5$ to $\tau = 6.5$) is due to a offset between the release of the LEV lift-augmentation effect and the TEV lift increasing effect.

(iii) The force drop in the next stage (e.g. from $\tau = 1$ to $\tau = 3$ and from $\tau = 6.5$

to $\tau = 7.5$) is owing to the newly formed LEV vortex pair squeezing away the main leading edge vortex that originally contributed to the large lift force. Moreover, the newly generated TEV also causes a large lift drop due to its downwash effect.

(iv) In low-level force equilibrium stage (e.g. from $\tau = 3$ to $\tau = 4.5$ and from $\tau = 7.5$ to $\tau = 9$), the lift keeps at a relative low stable value with slightly increase because of the growth of the secondary LEV pair and the TEV moving upstream to the upper surface.

The lift on the flap could be analyzed in a similar way. Unlike the lift acting on the main airfoil, the lift acting on the flap exhibits three stages in one period: the lift-reduction stage, the stable stage, and the lift-increase stage, which could be observed in Figure 12 (bottom). During the lift-reduction stage (e.g. from $\tau = 0$ to $\tau = 0.2$ and from $\tau = 3.8$ to $\tau = 5$), the TEV is blown away from the upper surface of the flap. In the stable stage (e.g. from $\tau = 1$ to $\tau = 3$ and from $\tau = 5$ to $\tau = 7$), the lift maintains a stable, low value, and the flow field consists of a complex interaction of the main and secondary LEVs and TEVs. After that is the lift-increase stage (e.g. $\tau = 3$ to $\tau = 3.8$ and from $\tau = 7$ to $\tau = 7.8$) when the TEV generated in the last stage moves upstream to the upper surface of the flap. The right columns of 13 and 14 show the spatial distribution of local vortex pressure lift due to vortices inside each grid cell at 8 typical instants $\tau_i = i$ $(i = 1, 2, ..., 8)$ for the flap. We could see from these figures that the lift on the flap is mainly caused by the main LEV and TEV as well as the vortex sheet in the boundary layer. While the secondary vortex structures contribute little lift to the flap.

Combining the vortex lift distribution in the right column of 13 and 14 with figure 12, we could analyze how the evolution of vortical structures in the flow field influences the lift acting on the flap.

(i) The flap lift decrease stage is related to the collapse of suction effect with blowing away of the TEV on the upper surface of the flap:

(ii) The stable stage is due to the newly formed TEV contributing to positive lift which compensates for the lift loss.

(iii) The flap lift increase stage could be explained by the suction mechanism caused by the growth of the TEV.

5. Summary

In this paper, the vortex force approach for viscous flows for multi-bodies has been developed. The lift and drag forces for each individual body in a multi-body configuration have been derived, with both pressure force (contributed by vorticity in the flow field and on the body surface) and viscous force included.

The pressure force contributed by vorticity in the flow field (also called vortex-pressure force) was found to be the dominant force and represented as the scalar product of the vortex-pressure force factor and the local flow velocity. The vortex-pressure force factors can be precomputed by solving a Laplace equation. Vortex-pressure force maps for for every individual body in the multi-body assembly were designed based on the vortex-pressure force factors for the purpose of identifying the force contribution of a given vortex in the flow field, and the positive and negative force generating directions were defined in these maps. Flow control strategies could be designed to maintain or create the lift-enhancing/drag-reducing vortex and to minimize the lift-reducing/drag-increasing vortex according to the vortex-pressure force maps, where the force contribution of each given vortex could be analyzed without pre-knowledge of the flow field. Another advantage of this vortex force map method for multi-bodies is its capability to extract force from limited/low-resolution flow data, e.g. PIV fields, in a non-invasive manner.

In order to illustrate the proposed vortex force decomposition method, analyses have

been made for an unsteady flow around wing-flap configurations. The force predictions arising from the current vortex force method have been shown to agree satisfactorily with those from CFD simulations. For both the main airfoil and the flap, we found that the dominant force was the vortex-pressure force. When the Reynolds number was large enough (greater than 1000), the pressure force contributed by the newly created vorticity on the body surface and the skin-friction force are negligible. The force oscillation behavior, as well as its relationship with the vortex flow pattern and vortex-pressure force map, have also been studied. The study of the spatial distribution of local vortex force due to vortices inside each grid cell provided additional evidence for those correlations. And it has been shown that the force acting on both the main airfoil and the flap is closely related to the vortex evolution near the wing-flap configuration. The spatial distribution of the vortex-pressure force analysis on the main airfoil showed that the four force stages, the LEV-augmentation stage; the high-level force equilibrium stage; the force drop stage; and the low-level force equilibrium stage, were highly related to the evolution of the vortical structures. Similarly the analysis of the spatial distribution of the vortex-pressure force on the flap showed the influence of the vortical structures on the three-stage force oscillation: the flap force increase stage was due to the collapse of the LEV suction; the force stable stage owed to a balance between the TEV force-enhancing effect and the suction loss of the LEV; the force increase stage was a result of the TEV suction effect.

In summary, we presented a force decomposition method for incompressible unsteady viscous flows applicable to a wide range of Reynolds numbers. The vortex-pressure force maps for each body among an assembly of bodies were built. As application, 2-D results of a wing-flap starting flow agreed well with CFD results. The theoretical appeal of this method lies in: 1. separating the body forces and providing links to the flow features (velocity and vorticity), which provides a better understanding of the origin of aerodynamic and hydrodynamic forces; 2. obtaining force directly from velocity field near the bodies. The method presented here can also be easily extended to the study of vortex torque as a future work.

Acknowledgements

This work has received funding from the European Union's Horizon 2020 research and innovation programme under the Marie Sklodowska-Curie grant agreement No.765579. This work was also funded by the Leverhulme Trust, Grant Ref ECF-2018-727. Their support is gratefully acknowledged.

Declaration of Interests

The authors report no conflict of interest.

REFERENCES

Alejandro, D. E. H., Mustafa, P., Matej, K. & Bas, V. O. 2018 Flow visualization around a flapping-wing micro air vehicle in free flight using large-scale piv. *Aerospace* **5** (4).

Ansari, S. A., Żbikowski, R. & Knowles, K. 2006 Non-linear unsteady aerodynamic model for insect-like flapping wings in the hover. part 2: Implementation and validation. *Proceedings of the Institution of Mechanical Engineers, Part G: Journal of Aerospace Engineering* **220** (3), 169–186.

Bai, C. Y., Li, J. & Wu, Z. N. 2014 Generalized kutta–joukowski theorem for multi-vortex and multi-airfoil flow with vortex production — a general model. *Chinese Journal of Aeronautics* **27** (5), 1037–1050.

Birch, J. M. & Dickinson, M. H. 2003 The influence of wing–wake interactions on the

production of aerodynamic forces in flapping flight. *Journal of experimental biology* **206** (13), 2257–2272.

Bird, H. J. A., Ramesh, K., Ōtomo, S. & Viola, I. M. 2022 Usefulness of inviscid linear unsteady lifting-line theory for viscous large-amplitude problems. *AIAA Journal* **60** (2), 598–609, arXiv: https://doi.org/10.2514/1.J060808.

Bomphrey, R. J., Nakata, T., Phillips, N. & Walker, S. M. 2017 Smart wing rotation and trailing-edge vortices enable high frequency mosquito flight. *Nature* **544**, 92—95.

Chang, C. C. 1992 Potential flow and forces for incompressible viscous flow. *Proceedings of the Royal Society of London. Series A: Mathematical and Physical Sciences* **437** (1901), 517–525.

Chang, C. C., Yang, S. H. & Chu, C. C. 2008 A many-body force decomposition with applications to flow about bluff bodies. *Journal of Fluid Mechanics* **600**, 95–104.

Cummins, C., Seale, M., Macente, A., Certini, D., Mastropaolo, E., Viola, I. M. & Nakayama, N. 2018 A separated vortex ring underlies the flight of the dandelion. *Nature* **562**, 414—-418.

Dong, J., Viré, A. & Li, Z. R. 2022 Analysis the vortex ring state and propeller state of floating offshore wind turbines and verification of their prediction criteria by comparing with a cfd model. *Renewable Energy* **184**, 15–25.

Ford, C. W. Pitt & Babinsky, H. 2013 Lift and the leading-edge vortex. *Journal of Fluid Mechanics* **720**, 280–313.

Howe, M. S. 1995 On the force and moment on a body in an incompressible fluid, with application to rigid bodies and bubbles at high and low reynolds numbers. *The Quarterly Journal of Mechanics and Applied Mathematics* **48** (3), 401–426.

Hsieh, C. T., Kung, C. F., Chang, C. C. & Chu, C. C. 2010 Unsteady aerodynamics of dragonfly using a simple wing–wing model from the perspective of a force decomposition. *Journal of fluid mechanics* **663**, 233–252.

Katz, J. & Plotkin, A. 2001 Low-speed aerodynamics: Second edition. *Cambridge University Press* .

Li, C., Dong, H. & Zhao, K. 2018 A balance between aerodynamic and olfactory performance during flight in drosophila. *Nature Communications* **9** (1).

Li, J., Wang, Y. N, Graham, J. M. R. & Zhao, X. W. 2020*a* Vortex moment map for unsteady incompressible viscous flows. *Journal of Fluid Mechanics* **891**, A13.

Li, J., Wang, Y. N., Graham, J. M. R. & Zhao, X. W. 2021 Evaluating unsteady fluid dynamic forces in viscous flows from the vorticity field. *AIAA Journal* **59** (1), 22–33, arXiv: https://doi.org/10.2514/1.J059575.

Li, J. & Wu, Z. N. 2018 Vortex force map method for viscous flows of general airfoils. *Journal of Fluid Mechanics* **836**, 145–166.

Li, J., Zhao, X. W. & Graham, J. M. R. 2020*b* Vortex force maps for three-dimensional unsteady flows with application to a delta wing. *Journal of Fluid Mechanics* **900**, A36.

Li, X. & Feng, L. H. 2022 Critical indicators of dynamic stall vortex. *Journal of Fluid Mechanics* **937**, A16.

Lin, J. C. & Rockwell, D. 1996 Force identification by vorticity fields: techniques based on flow imaging. *Journal of Fluids and Structures* **10** (6), 663–668.

Liu, K., Zhang, B.F., Zhang, Y.C. & Zhou, Y. 2021 Flow structure around a low-drag ahmed body. *Journal of Fluid Mechanics* **913**, A21.

Milne-Thomson, L. M. 1960 Theoretical hydrodynamics london macmillan & co ltd. chap. 5,9,13.

Moreau, J. J. 1952 *Bilan dynamique d'un écoulement rotationnel....* Gauthier-Villars.

Noca, F. 1996 On the evaluation of instantaneous fluid-dynamic forces on a bluff body .

Noca, F., Shiels, D. & Jeon, D. 1997 Measuring instantaneous fluid dynamic forces on bodies, using only velocity fields and their derivatives. *Journal of Fluids and Structures* **11** (3), 345–350.

Norberg, C. 2003 Fluctuating lift on a circular cylinder: review and new measurements. *Journal of Fluids and Structures* **17** (1), 57–96.

Ploumhans, P., Winckelmans, G. S., Salmon, J. K., Leonard, A. & Warren, M. S. 2002 Vortex methods for direct numerical simulation of three-dimensional bluff body flows:

application to the sphere at re= 300, 500, and 1000. *Journal of Computational Physics* **178** (2), 427–463.

Polhamus, E. C. 1966 A concept of the vortex lift of sharp-edge delta wings based on a leading-edge-suction analogy. *NACA Technical Note* **D** (3767).

Saffman, P. G. 1995 *Vortex dynamics*. Cambridge university press.

Shew, W. L., Poncet, S. & Pinton, J. F. 2006 Force measurements on rising bubbles. *Journal of Fluid Mechanics* **569**, 51–60.

Streitlien, K. & Triantafyllou, M. S. 1995 Force and moment on a joukowski profile in the presence of point vortices. *AIAA journal* **33** (4), 603–610.

Usherwood, J. R., Cheney, J. A., Song, J. L., Windsor, S. P., Stevenson, J. P. J., Dierksheide, U., Nila, A. & Bomphrey, R. J. 2020 High aerodynamic lift from the tail reduces drag in gliding raptors. *Journal of Experimental Biology* **223** (3).

WANG, Z. J. 2005 Dissecting insect flight. *Annual Reviews on Fluid Mechanics* **37**.

Wu, T. Y. 2011 Fish swimming and bird/insect flight. *Annual Review of Fluid Mechanics* **43** (1), 25–58, arXiv: https://doi.org/10.1146/annurev-fluid-122109-160648.

Xia, X. & Mohseni, K. 2013 Lift evaluation of a two-dimensional pitching flat plate. *Phys. Fluids* **25**, 091901.

Zhu, G., Bearman, P. W. & Graham, J. M. R. 2002 Prediction of drag and lift using velocity and vorticity fields. *The Aeronautical Journal* **106** (1064), 547–554.

Zhu, G., Bearman, P. W. & Graham, J. M. R. 2007 Prediction of drag and lift of wings from velocity and vorticity fields. *The Aeronautical Journal* **111** (1125), 699–704.